iScience

CellPress
OPEN ACCESS

Article

First principles investigation of screened Coulomb interaction and electronic structure of low-temperature phase TaS_2

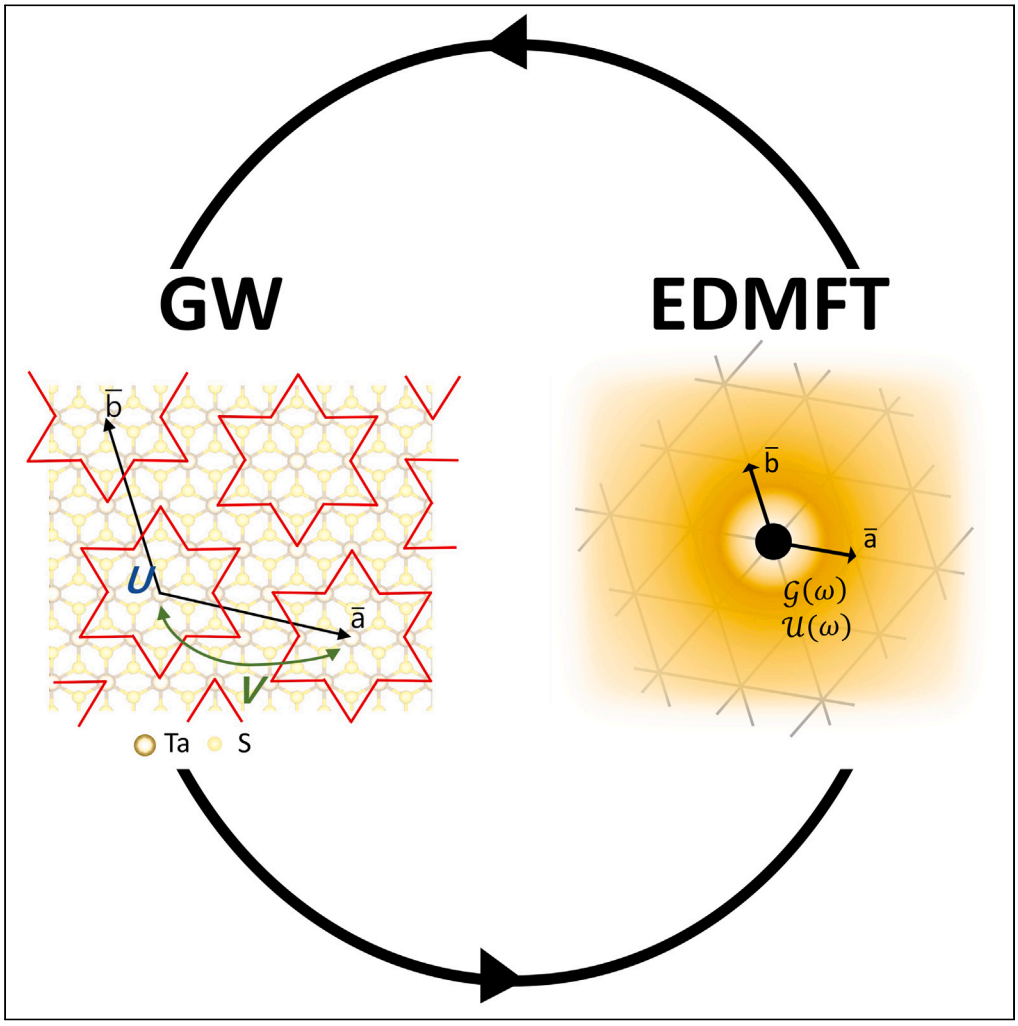

Taek Jung Kim,
Min Yong Jeong,
Myung Joon Han

mj.han@kaist.ac.kr

Highlights

Local, non-local interaction and electronic structure of TaS_2 studied by GW+EDMFT

Local and non-local Coulomb interaction are estimated and the electronic properties are discussed

Kim et al., iScience 26, 106681
May 19, 2023
https://doi.org/10.1016/j.isci.2023.106681

iScience

CellPress
OPEN ACCESS

Article

First principles investigation of screened Coulomb interaction and electronic structure of low-temperature phase TaS_2

Taek Jung Kim,[1] Min Yong Jeong,[1] and Myung Joon Han[1,2,*]

SUMMARY

By means of *ab initio* computation schemes, we examine the electronic screening, Coulomb interaction strength, and the electronic structure of a quantum spin liquid candidate monolayer TaS2 in its low-temperature commensurate charge-density-wave phase. Not only local (U) but non-local (V) correlations are estimated within random phase approximation based on two different screening models. Using GW + EDMFT (GW plus extended dynamical mean-field theory) method, we investigate the detailed electronic structure by increasing the level of non-local approximation from DMFT ($V = 0$) to EDMFT and GW + EDMFT.

INTRODUCTION

Understanding the effect of Coulombic interaction between electrons in solid has long been a central theme of condensed matter physics.[1] Notably, the relevant material systems are being extended to include various two-dimensional (2D) van der Waals materials[2–9] and more recently their twisted combinations.[10–18] The local on-site interaction (conventionally represented by U in Hubbard model) can induce electron localization, magnetic moment and thereby leading to metal-to-insulator and magnetic phase transition.[1,19–21] Many of most intriguing phenomena have been explored within this picture such as unconventional superconductivity and quantum spin liquid.[21–26] Non-local Coulomb interaction (denoted by V in extended Hubbard model) also plays an important role. For example, it can enhance the itinerancy of electrons by screening Coulomb interactions or broadening the effective bandwidth.[27,28] Out of its competition and cooperation with electron hoppings and local correlations, various instabilities can be induced toward the charge-ordered or charge density wave (CDW) phase and many others including high angular momentum superconductivity.[27–37] Recently, the effect of non-local Coulomb interaction receives increasing attention in 2D material.[6,38–41]

Among many correlated van der Waals materials, TaS_2 provides an intriguing case by displaying multiple ordered phases and their transitions.[42–45] At high temperature, TaS_2 is known to be metallic and has 1T structure shown in Figure 1A. As temperature is lowered, it exhibits so-called 'nearly commensurate CDW (NCCDW)', and then finally becomes insulating.[46,47] Superconductivity is also observed below $T_C \approx 2 - 5$ K by applying pressure, doping or electric field.[42–44] Importantly, the stabilization of the low temperature insulating phase is accompanied by commensurate CDW (CCDW) transition for which the long-range 'star of David (SOD)' pattern of atomic rearrangement is well identified in both experiments and simulations (see Figures 2A and 2B).[46–50] This phase hosts a flat band in the close vicinity of chemical potential because of the reduced hopping integral in between SOD molecular orbitals. Therefore, unveiling the electronic property of CCDW SOD phase is important to understand the metal-insulator transition and the other related phases observed or suggested in this material at low temperature.[42–45,51–53] Given that Ta atom has the 4+ formal valance, the SOD unit cell should have odd number of electrons (*i.e.*, $13 = 5d^1 \times 13$), and CCDW-TaS_2 is expected to be metallic according to the standard band picture. It is however in a sharp contrast to experiments.[54] Several recent studies focusing on this issue suggested that either Mott mechanism or interlayer dimerization is responsible for metal-to-insulator transition.[45,55–61] The important challenge here is to estimate the strengths of Coulomb interactions.[62]

Another intriguing possibility in this material is quantum spin liquid (QSL). By noting that the low-temperature CCDW phase forms a triangular lattice and carries nominally S = ½ local moment, the low

[1]Department of Physics, Korea Advanced Institute of Science and Technology (KAIST), Daejeon 34141, Republic of Korea

[2]Lead contact

*Correspondence: mj.han@kaist.ac.kr

https://doi.org/10.1016/j.isci.2023.106681

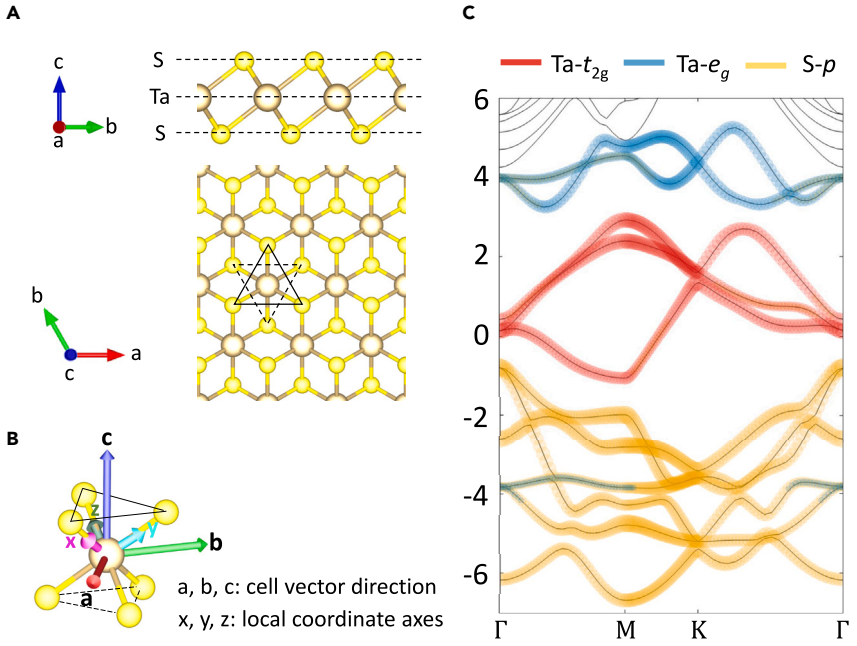

Figure 1. Crystal and electronic structure of 1T-TaS_2

(A) Crystal structure of monolayer 1T-TaS_2. The side and top view is presented above and below, respectively. As shown in the side view, a layer consists of S-Ta-S layer. In the top view, the triangle (solid line) and inverted triangle (dotted line) indicates the S atoms around Ta in the upper and the lower layers, respectively.

(B) The local environment around Ta. The Ta atom is surrounded by six S atoms forming the octahedral structure with slight trigonal distortion. The red, green, and blue arrow (a, b, and c vectors) indicates the three cell vectors shown in (A). The magenta, cyan, and olive colored arrow shows the local coordinate axes for Ta-d orbital projection. Local axes point to the octahedral directions by neglecting the small trigonal distortion.

(C) The orbital-projected band structure of 1T-TaS2. Blue and red color shows the Ta-t_{2g} and Ta-e_g orbital contribution, respectively, and yellow refers to the *p* orbital contribution of S atoms.

temperature TaS_2 was suggested as a QSL candidate.[51] This idea is supported by the absence of long-range magnetic order down to low temperature and the gapless spin excitations.[51–53] Notably, a recent study highlights the effect of non-local Coulomb interaction (*V*) on the magnetic nature related to QSL.[63]

In this paper, we examine the detailed electronic behaviors of monolayer TaS_2. Based on two different models, the electronic screenings are taken into account within random phase approximation (RPA). Correlation strengths, in terms of both on-site *U* and inter-site *V*, are successfully quantified for the low-temperature CCDW phase. By adopting GW + EDMFT,[32,64–69] we calculate the electronic structure with three different levels of approximation for inter-site correlation. Although the Mott gap is mainly governed by the local interaction, non-local Coulomb interaction is also sizable. Its effect on the electronic screening, band dispersion and another possibility toward charge-ordered phase are discussed.

RESULTS AND DISCUSSION

Non-interacting band structure and tight-binding parameters

Figures 1A and 1B shows the crystal structure of 1T-TaS_2 and the local TaS_6 unit, respectively. The corresponding non-interacting band structure within generalized gradient approximation (GGA; *i.e.*, $U = V = 0$ eV) is presented in Figure 1C where different colors represent the different orbital characters as projected onto the local coordinates as defined in Figure 1B. Ta-t_{2g} states dominate the near Fermi energy (E_F) region and the t_{2g}^1 configuration is well identified. The higher energy bands above + 3 eV and below − 1 eV are mainly composed of Ta-e_g and S-*p* character, respectively, whereas the greenish bands reflect the mixture of Ta-e_g and S-*p*. The overall electronic feature is in good agreement with previous studies.[56,70–72]

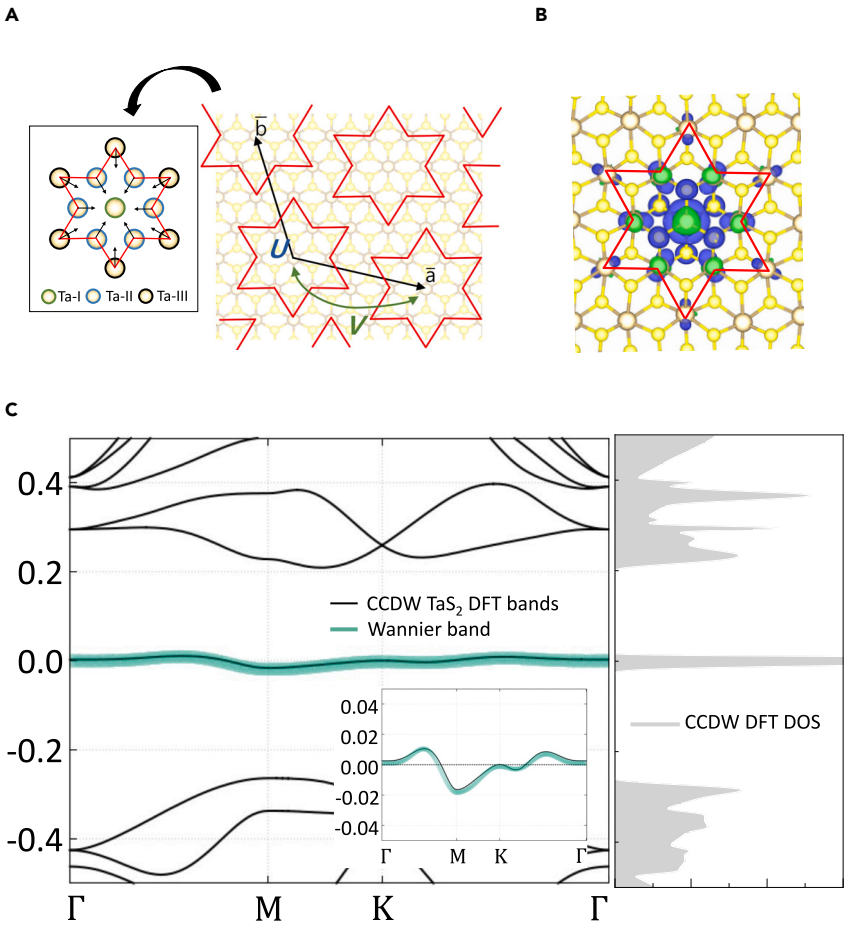

Figure 2. Crystal and electronic structure of CCDW-TaS_2

(A) Crystal structure of CCDW phase of TaS_2. Twelve Ta atoms move toward the central Ta, forming a SOD unit (inset) and a molecular orbital at around the center. *U* and *V* refers to the on-site and the inter-site Coulomb interaction of the molecular orbital, respectively. $\bar{a}$ and $\bar{b}$ are the unit cell vectors corresponding to CCDW phase.

(B) The calculated MLWF for the SOD molecular orbital in CCDW-TaS_2. Red line depicts the SOD unit.

(C) The calculated DFT band structure (left; black line) and its density of state (right). The overlaid green line shows the band structure of MLWF for SOD molecular orbital. The inset shows the zoom-in figure near E_F.

By lowering temperature, 1T-TaS_2 is known to undergo CDW structural transitions. So-called nearly commensurate charge density wave (NCCDW) phase is stabilized below $T \approx 350$ K and followed by CCDW at $T \approx 180$ K.[46–48] Figure 2A depicts the CCDW structure, so-called SOD pattern, in which twelve Ta atoms move toward the central one forming a 13-Ta-atom unit cluster.[46,47,73,74] In this phase, the band structure also changes accordingly.[55,56,75,76] As shown in Figure 2C, a well-separated single electron band is solely responsible for the low energy region near E_F whereas six bonding orbital states are fully occupied by twelve Ta-*d* electrons well below E_F. It is noted that the near E_F band is fairly flat and nondispersive. It is therefore prone to metal-to-insulator transition and other exotic possibilities such as quantum spin liquid phase when interactions come in to play.[55,56,75,76]

The green-colored line in Figure 2C shows the band produced by maximally localized Wannier function (MLWF)[77,78] based on which we estimated a reliable set of parameters for the low energy effective (non-interacting) Hamiltonian of CCDW-TaS_2. Its real space visualization is given in Figure 2B. The calculated TB parameters are as follow: the first and the second neighbor hopping is $|t_1| = 1.812$ and $|t_2| = 0.814$ meV, respectively, well compared with the previous reports.[63,79] It is interesting to note that the third neighbor hopping $|t_3| = 1.785$ meV is larger than $|t_2|$ and comparable with $|t_1|$.[63]

Table 1. Estimated Coulomb interactions for CCDW-TaS_2

	3 bands (RPA)	5 bands (cRPA)
U (eV)	0.371	0.653
V (eV)	0.208	0.359

The calculated on-site (U) and inter-site Coulomb interaction (V) corresponding to the SOD CDW phase. The parameters are estimated from two different approaches as discussed in the main text.

The estimation of on-site and inter-site correlation

Now we try to calculate the interaction parameters from first-principles. Quantitative information of correlation strength is often crucial for exploring the possible exotic quantum phases and understanding their properties. In the debate over the band gap origin of TaS_2,[45,55–61] for example, the size of on-site U is of key importance. Non-local V is of particular interest in the systems close to the CDW instability as it can induce charge-ordering instability in the extended Hubbard systems.[27,32,80] In general, the constructed phase diagrams can be qualitatively different depending on the non-local term. As such, there have been several attempts to directly estimate the interaction strengths of various transition metal dichalcogenides (TMDs).[2,55,81–85] However, *ab initio* calculation of these parameters corresponding to CDW phase is challenging especially for non-local V.

We calculate both U and V for CCDW-TaS_2 based RPA/cRPA method. Ideally, it is desirable to compute these parameters from the direct cRPA calculation of CCDW unitcell. However, a difficulty arises from the demanding computation cost in dealing with the large cell size. Here we extract the interaction parameters from the undistorted 1T-structure,[55,86] and consider two different approaches. First, the CCDW U value can be estimated as the average of atomic Coulomb interactions of 1T structure whose screening process can be considered within RPA. This first way of computation gives rise to:

$$U = \frac{1}{13^2}\sum_{R,R'\in\bigstar} U_{R-R'} \qquad \text{(Equation 1)}$$

where $U_{R-R'}$ is the Fourier transformed leading eigenvalue of RPA-screened Coulomb matrix. Namely, $U_{R-R'} = \frac{1}{N_q}\sum_q U_q e^{iq\cdot(R-R')}$ where $U_q = \max \lambda_q$, and λ_q is the eigenvalue of RPA-screened Coulomb matrix $\mathcal{W}_{II}^{\mathcal{RPA}}$ represented in the eigenbasis of bare Coulomb matrix.[86] The screened Coulomb matrix is calculated for t_{2g} manifold; namely, the red-colored bands in Figure 1C. R and R′ are the lattice cell vectors corresponding to 1T structure, and q is the lattice momentum. N_q is the grid number of lattice momentum. The white-star symbol represents the ★ indices of Ta atoms in the same SOD (which is composed of 13 Ta atoms; see Figure 2A). In this first approach, the inter-site correlation V is also computed within the same spirit:

$$V = \frac{1}{13^2}\sum_{R\in\bigstar,R'\in\bigstar} U_{R-R'} \qquad \text{(Equation 2)}$$

where the black-star symbol ★ refers to the indices of Ta atoms belonging to the nearest-neighboring SOD (indicated by the unit cell vector $\bar{a}$ and $\bar{b}$ in Figure 2A). The calculated U and V following this first approach are presented in Table 1; referred to as '3 bands (RPA)'.

The second approach considers the weights of Ta atoms by projecting them onto the CCDW molecular orbital. This idea itself is not necessarily combined with (c)RPA but can go with any other method of computing atomic Coulomb interaction $\overline{U}^{LR}$.[55] The molecular orbital U then can be estimated from the atomic Ta-$d\overline{U}^{LR}$: By calculating the projected weights of Ta-d orbitals ($|d_a\rangle$) with respect to CCDW molecular orbitals ($|\Psi\rangle$),

$$\frac{U}{\overline{U}^{LR}} = \sum_{a\in\bigstar}|\langle d_a|\Psi\rangle|^4 \qquad \text{(Equation 3)}$$

where a is the atomic Ta index. Ta atoms are classified into three different types considering their symmetry (see the inset of Figure 2A). Our calculations give rise to $|\langle d_a|\Psi\rangle|^2 = 0.229, 0.064$ and 0.035 for Ta-I, Ta-II, and Ta-III, respectively. U and V are obtained as follow:

$$U = \sum_{R,R' \in \bigstar} |\langle d_R|\Psi\rangle|^2 |\langle d_{R'}|\Psi\rangle|^2 \overline{U}_{R-R'} \quad \text{(Equation 4)}$$

$$V = \sum_{R \in \bigstar, R' \in \bigstar} |\langle d_R|\Psi\rangle|^2 |\langle d_{R'}|\Psi\rangle|^2 \overline{U}_{R-R'} \quad \text{(Equation 5)}$$

Here we calculate $\overline{U}_{R-R'}$ based on cRPA. In Table 1, this set of results are denoted by '5 bands (cRPA)' as 5-band model of 1T-TaS_2 (both t_{2g} and e_g) is adopted.

The calculation results are summarized in Table 1. The U values are different in two different approaches: U = 0.371 eV from '3-band RPA' and 0.653 eV from '5-band cRPA'. It is not surprising but rather expected because different 'models' shall take care of different screenings. For example, the weaker correlation in the former model is naturally attributed to the more screening channels taken into account. Both results therefore carry useful information for further study whereas the larger supercell of CCDW phase is not directly computable within cRPA. It is also noted that our results are considerably larger than that of a previous study based on linear response calculation; U = 0.180 eV.[55] From the point of view of the extracting method of CCDW-U value from 1T structure, the previous study by Darancet et al.[55] is the same with our second approach (*i.e.*, 'five-band model'). Thus the ~0.5 eV difference certainly reflects the difference between the linear response adopted by Darancet et al.[55] and our RPA method whereas only the latter takes the electronic screenings into account directly. Interestingly, however, the calculated atomic U itself (that is, corresponding to Ta-d on-site interaction) is larger in the linear response calculation, $\overline{U}^{LR}$ = 2.27 eV,[55] than our cRPA $\overline{U}_{R-R'=0}$ = 1.83 eV. It is therefore indicative of that the difference is not simply attributed to the difference between cRPA and linear response. We presume that the projection also plays an important role. As shown in Equation 4, our projection method not just takes all of Equation 3 portions into account but it also includes some inter-site contributions between different Ta atoms in an SOD molecular orbital.

It is also useful to compare the correlation strength of TaS_2 to that of $NbSe_2$. A previous study of Kamil et al.[86] reports U = 0.3 eV for $NbSe_2$ and their estimation was based on RPA and three-band model, corresponding to our first approach. It is noted that U for CCDW-TaS_2 is significantly larger than CCDW-$NbSe_2$ by about 0.07 eV (see Table 1), which is likely attributed to the different screenings as discussed in the previous studies on the comparison of $TaSe_2$ with TaS_2.[85,87] Here we also note that a recent ARPES study suggests the weaker correlation for $NbSe_2$ than $TaSe_2$.[88]

Table 1 also presents the inter-site correlation strength V which can be important for understanding the possible exotic phases relevant to this system, but has not been quantitatively estimated before. First of all, sizable V value is noticed; ~50% of on-site correlation in both models. It can therefore be important to take this effect into account within the extended Hubbard model. It is obvious that Hubbard-type correlation is indispensable for overcoming the DFT-GGA limitation which gives rise to metallic band structure.[54] Previous theoretical studies showed that the inclusion of on-site correlation within DFT+ U and single-site DMFT indeed well reproduces the insulating state even though the former incorrectly predicts the magnetically ordered ground state.[55,56] According to the DMFT calculation, Mott transition starts to occur at U ~0.7 eV in bulk TaS_2.[56] Note that both sets of our results in Table 1 provide the large enough interaction U with respect to the bandwidth $W \sim 9|t| \sim 0.02$ eV. Importantly, however, the effect of non-local V has remained unexplored.

GW + EDMFT electronic structure

To see the effect of both local U and non-local V on the electronic structure, one needs to go beyond the single-site DMFT. Here we adopt GW + EDMFT for that purpose. Computation details are given in STAR Methods. In Figures 3A–3C, we present the calculated spectral functions as obtained by analytic continuation of Matsubara Green function using maximum entropy method.[89–91] In sharp contrast to the metallic DFT-GGA band structure, GW + EDMFT result clearly shows the insulating gap being consistent with experiment, DFT+ U and single-site DMFT. In the case of DFT+ U, the long-range spin order naturally comes in as the ground state configuration.[55] With our first set of interaction parameters (U = 0.371 eV, V = 0.208 eV; shown in Figures 3A and 3B), the upper and the lower Hubbard peak is observed at about ±0.2 eV, respectively, which is well compared with a recent STM experiment of monolayer TaS_2.[54,69] Another set of 5-band model produces a slightly larger gap as presented in Figure 3C. Although this stronger correlation set of parameters also reproduces the insulting phase as expected, the notable difference is

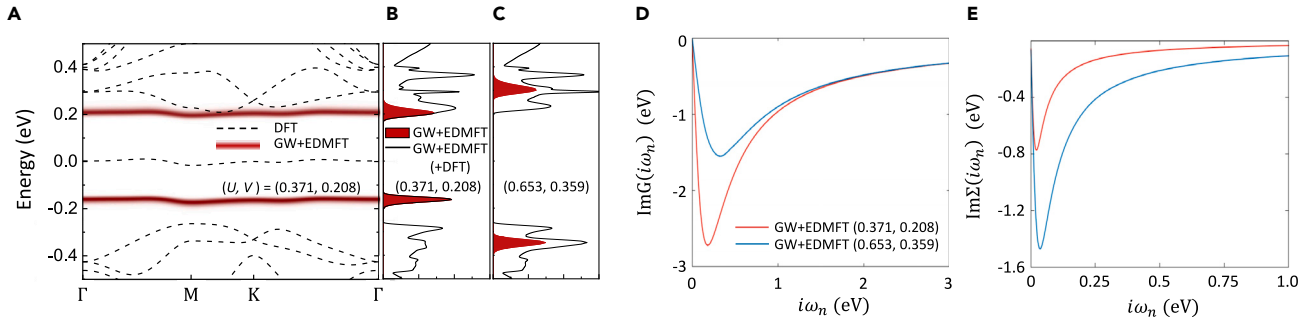

Figure 3. Results of GW + EDMFT calculations

(A) The momentum-dependent spectral function calculated by DFT-GGA (dashed lines) and GW + EDMFT (red line). The estimated Coulomb interaction parameters from 3-band model were used as given in parentheses (U, V).

(B and C) The momentum-integrated spectral function of GW + EDMFT. Coulomb interactions are estimated by (B) 3-band and (C) 5-band model. The red colored data represent the density of states (DOS) of GW + EDMFT, and the black lines show the DOS sum of GW + EDMFT and DFT.

(D and E) The calculated imaginary part of local (D) Green function and (E) self-energy of GW + EDMFT. The red and blue color refers to the two different interaction parameter sets as given in the parentheses.

the position of Hubbard bands which are in this case found inside the uncorrelated states (thin black line). The detailed spectroscopic characterization of the valence and conduction band can therefore be useful to determine the correlation strength whereas the band gap size itself is probably too small to be precisely compared.

To unveil the other aspects of electronic correlations, we present the imaginary part of local Green function in Figure 3D. With both parameter sets, it is clearly observed that Im $G(i\omega_n)$ goes to zero as $i\omega_n \rightarrow 0$, indicative of the zero spectral weight at E_F, namely, the insulating phase. From the fact that minimum frequency point is lower in the 3-band-model case (red line), it also confirms the observed gap size difference in Figures 3A–3C. The calculated self-energies highlight the same feature: In Figure 3E, the slope of $\partial \mathrm{Im}\Sigma / \partial\omega_n$ at $i\omega_n \rightarrow 0$ shows the vanishing quasiparticle weight $Z = \left[1 - \frac{\partial \mathrm{Im}\Sigma}{\partial \omega_n}\right]^{-1} \approx 0$, indicating Mott phase.

Further examination of screened coulomb interactions

To gain further insights on the electronic correlations, we investigate the screened Coulomb interaction and the charge susceptibility. Figure 4A shows the real part of screened Coulomb interaction W_{loc}. The effect of non-local Coulomb interaction can be systematically examined by changing the level of

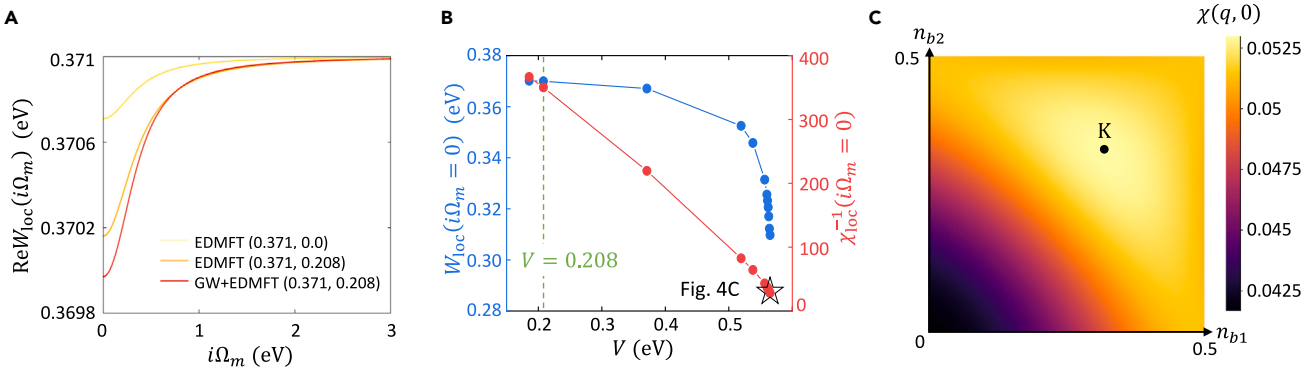

Figure 4. Bosonic quantities from GW + EDMFT

(A) The screened Coulomb interaction W calculated by DMFT (yellow; $V = 0$), EDMFT (orange), and GW + EDMFT (red).

(B) The static part of $W(i\Omega_m = 0)$ (blue-colored; left yaxis) and χ^{-1}_{loc} (red-colored; right yaxis) as a function of V. The 3-band RPA estimation of V is indicated by vertical green-dotted line.

(C) The momentum-dependent charge susceptibility $\chi(q, i\Omega_m = 0)$ in the vicinity of charge-ordered phase. The calculation has been conducted with $(U, V) = (0.371\ \mathrm{eV}, 0.565\ \mathrm{eV})$ indicated by black-star symbol in (B).

approximations. Here we fix the value of on-site interaction U = 0.371 eV, and compare the results of two different inter-site V = 0 and 0.208 eV. GW self-energy can also be taken into account on top of that. In high-frequency limit, the effective Coulomb interaction approaches to its 'bare' value U = 0.371 eV in all three cases. In low frequency limit, W_{loc} gradually decreases as the more non-local interactions get involved. It is a general feature of extended Hubbard model[27,32] although the screening effect by V is not significant as the charge fluctuation is largely suppressed in Mott phase. Figure 4B also shows that $W(i\Omega_m = 0)$ gradually decreases as V increases whereas it does not vary much when V is small.

In large V limit, on the other hand, its effect can become pronounced. As shown in Figure 4B, the screened Coulomb interaction is significantly reduced, indicating that charge fluctuations caused by Vfurther screen the Coulomb interactions.[27,32] In this regime of $V \gtrsim 0.5$ eV, W gets rapidly reduced, and simultaneously, the local charge susceptibility diverges (red line):[27,32]

$$\chi_{loc}^{-1} \rightarrow 0 \qquad \text{(Equation 6)}$$

where $\chi_{loc} = \frac{1}{N_q}\sum_q \chi(q)$ and $\chi(q) = (-P(q, i\Omega_m)[1 - v(q)P(q, i\Omega_m)]^{-1})_{i\Omega_m = 0}$. To perform the detailed investigation of this limit, we calculate the momentum-dependent static charge susceptibility at V = 0.565 eV which is deemed a point close enough to the charge-ordering-type instability (corresponding to the black star point in Figure 4B). In Figure 4C, a diverging feature is clearly identified at (n_{b_1}, n_{b_2})=(0.333,0.333) indicative of a charge-ordering instability (n_{b_i} is fractional coordinate of reciprocal lattice vector b_i). Although it implies the further charge instability over the CCDW phase, the critical V value is far from being realistic in the current system.

Conclusions

We investigated the electronic screening and the spectral property of monolayer TaS_2 by the combination of DFT, RPA, MLWF and GW + EDMFT. Both on-site and inter-site correlation strengths are estimated based on two different *ab initio* RPA approaches. Although its Mott insulating gap is mainly determined by on-site interaction, the inter-site V is also found to be sizable. The comparison of DMFT, EDMFT, and GW + EDMFT exhibits a systematic change of the electronic behavior because the levels of non-local self-energy computations are varied. Our work provides useful information and insight for understanding TaS_2 and the other related systems.

Limitations of the study

Our computations of screened Coulomb interaction are based on random phase approximation. The electronic structure calculations take account of non-local as well as dynamical self-energy within GW + EDMFT. The singlet formation caused by interlayer dimerization[57,59,92,93] could not be considered in our calculation setups.

STAR★METHODS

Detailed methods are provided in the online version of this paper and include the following:

- KEY RESOURCES TABLE
- RESOURCE AVAILABILITY
  - Lead contact
  - Materials availability
  - Data and code availability
- METHOD DETAILS
  - DFT and extended hubbard model construction
  - GW + EDMFT

ACKNOWLEDGMENTS

T.J.K. thanks Sangkook Choi for useful discussion of GW + EDMFT code implementations and Siheon Ryee for the useful tips on the convergence issues. This work was supported by the National Research Foundation of Korea (NRF) grant funded by the Korea government (MSIT) (Grant Nos.2021R1A2C1009303 and NRF-2018M3D1A1058754).

AUTHOR CONTRIBUTIONS

T.J.K. performed (c)RPA, EDMFT and GW + EDMFT calculations, and M.Y.J. conducted DFT and MLWF calculations. M.J.H. supervised the project. All authors participated in the interpretation of the data and wrote the manuscript.

DECLARATION OF INTERESTS

The authors declare no competing interests.

Received: December 30, 2022
Revised: March 28, 2023
Accepted: April 12, 2023
Published: April 18, 2023

REFERENCES

1. Imada, M., Fujimori, A., and Tokura, Y. (1998). Metal-insulator transitions. Rev. Mod. Phys. *70*, 1039–1263. https://doi.org/10.1103/RevModPhys.70.1039.

2. van Loon, E., Rösner, M., Schönhoff, G., Katsnelson, M.I., and Wehling, T.O. (2018). Competing Coulomb and electron–phonon interactions in NbS_2. npj Quant Mater *3*, 1–8. https://doi.org/10.1038/s41535-018-0105-4.

3. Zhang, Y., Lu, H., Zhu, X., Tan, S., Feng, W., Liu, Q., Zhang, W., Chen, Q., Liu, Y., Luo, X., et al. (2018). Emergence of Kondo lattice behavior in a van der Waals itinerant ferromagnet, Fe_3GeTe_2. Sci. Adv. *4*, eaao6791. https://doi.org/10.1126/sciadv.aao6791.

4. Kim, H.-S., Haule, K., and Vanderbilt, D. (2019). Mott metal-insulator transitions in pressurized layered trichalcogenides. Phys. Rev. Lett. *123*, 236401. https://doi.org/10.1103/PhysRevLett.123.236401.

5. Kang, S., Kim, K., Kim, B.H., Kim, J., Sim, K.I., Lee, J.-U., Lee, S., Park, K., Yun, S., Kim, T., et al. (2020). Coherent many-body exciton in van der Waals antiferromagnet $NiPS_3$. Nature *583*, 785–789. https://doi.org/10.1038/s41586-020-2520-5.

6. van Loon, E., Schüler, M., Springer, D., Sangiovanni, G., Tomczak, J.M., and Wehling, T.O. (2020). Coulomb engineering of two-dimensional Mott materials. Preprint at arXiv. https://doi.org/10.48550/arXiv.2001.01735.

7. Vaňo, V., Amini, M., Ganguli, S.C., Chen, G., Lado, J.L., Kezilebieke, S., and Liljeroth, P. (2021). Artificial heavy fermions in a van der Waals heterostructure. Nature *599*, 582–586. https://doi.org/10.1038/s41586-021-04021-0.

8. Kim, T.J., Ryee, S., and Han, M.J. (2022). Fe_3GeTe_2: a site-differentiated Hund metal. npj Comput. Mater. *8*, 245. https://doi.org/10.1038/s41524-022-00937-x.

9. Kiem, D.H., Jeong, M.Y., Yoon, H., and Han, M.J. (2022). Strain engineering and the hidden role of magnetism in monolayer VTe_2. Nanoscale *14*, 10009–10015. https://doi.org/10.1039/D2NR03026H.

10. Cao, Y., Fatemi, V., Demir, A., Fang, S., Tomarken, S.L., Luo, J.Y., Sanchez-Yamagishi, J.D., Watanabe, K., Taniguchi, T., Kaxiras, E., et al. (2018). Correlated insulator behaviour at half-filling in magic-angle graphene superlattices. Nature *556*, 80–84. https://doi.org/10.1038/nature26154.

11. Cao, Y., Fatemi, V., Fang, S., Watanabe, K., Taniguchi, T., Kaxiras, E., and Jarillo-Herrero, P. (2018). Unconventional superconductivity in magic-angle graphene superlattices. Nature *556*, 43–50. https://doi.org/10.1038/nature26160.

12. Yankowitz, M., Chen, S., Polshyn, H., Zhang, Y., Watanabe, K., Taniguchi, T., Graf, D., Young, A.F., and Dean, C.R. (2019). Tuning superconductivity in twisted bilayer graphene. Science *363*, 1059–1064. https://doi.org/10.1126/science.aav1910.

13. Burg, G.W., Zhu, J., Taniguchi, T., Watanabe, K., MacDonald, A.H., and Tutuc, E. (2019). Correlated insulating states in twisted double bilayer graphene. Phys. Rev. Lett. *123*, 197702. https://doi.org/10.1103/PhysRevLett.123.197702.

14. Liu, X., Hao, Z., Khalaf, E., Lee, J.Y., Ronen, Y., Yoo, H., Haei Najafabadi, D., Watanabe, K., Taniguchi, T., Vishwanath, A., and Kim, P. (2020). Tunable spin-polarized correlated states in twisted double bilayer graphene. Nature *583*, 221–225. https://doi.org/10.1038/s41586-020-2458-7.

15. Shen, C., Chu, Y., Wu, Q., Li, N., Wang, S., Zhao, Y., Tang, J., Liu, J., Tian, J., Watanabe, K., et al. (2020). Correlated states in twisted double bilayer graphene. Nat. Phys. *16*, 520–525. https://doi.org/10.1038/s41567-020-0825-9.

16. Cao, Y., Rodan-Legrain, D., Rubies-Bigorda, O., Park, J.M., Watanabe, K., Taniguchi, T., and Jarillo-Herrero, P. (2020). Tunable correlated states and spin-polarized phases in twisted bilayer–bilayer graphene. Nature *583*, 215–220. https://doi.org/10.1038/s41586-020-2260-6.

17. Wang, L., Shih, E.-M., Ghiotto, A., Xian, L., Rhodes, D.A., Tan, C., Claassen, M., Kennes, D.M., Bai, Y., Kim, B., et al. (2020). Correlated electronic phases in twisted bilayer transition metal dichalcogenides. Nat. Mater. *19*, 861–866. https://doi.org/10.1038/s41563-020-0708-6.

18. Xu, S., Al Ezzi, M.M., Balakrishnan, N., Garcia-Ruiz, A., Tsim, B., Mullan, C., Barrier, J., Xin, N., Piot, B.A., Taniguchi, T., et al. (2021). Tunable van Hove singularities and correlated states in twisted monolayer–bilayer graphene. Nat. Phys. *17*, 619–626. https://doi.org/10.1038/s41567-021-01172-9.

19. Dagotto, E. (1994). Correlated electrons in high-temperature superconductors. Rev. Mod. Phys. *66*, 763–840. https://doi.org/10.1103/RevModPhys.66.763.

20. Dagotto, E. (2005). Complexity in strongly correlated electronic systems. Science *309*, 257–262. https://doi.org/10.1126/science.1107559.

21. Lee, P.A., Nagaosa, N., and Wen, X.-G. (2006). Doping a Mott insulator: physics of high-temperature superconductivity. Rev. Mod. Phys. *78*, 17–85. https://doi.org/10.1103/RevModPhys.78.17.

22. Scalapino, D.J. (2012). A common thread: the pairing interaction for unconventional superconductors. Rev. Mod. Phys. *84*, 1383–1417. https://doi.org/10.1103/RevModPhys.84.1383.

23. Zhou, Y., Kanoda, K., and Ng, T.-K. (2017). Quantum spin liquid states. Rev. Mod. Phys. *89*, 025003. https://doi.org/10.1103/RevModPhys.89.025003.

24. Norman, M. (2016). Colloquium: herbertsmithite and the search for the quantum spin liquid. Rev. Mod. Phys. *88*, 041002. https://doi.org/10.1103/RevModPhys.88.041002.

25. Varma, C.M. (2020). Colloquium: linear in temperature resistivity and associated mysteries including high temperature superconductivity. Rev. Mod. Phys. *92*, 031001. https://doi.org/10.1103/RevModPhys.92.031001.

26. Salamon, M.B., and Jaime, M. (2001). The physics of manganites: structure and transport. Rev. Mod. Phys. *73*, 583–628. https://doi.org/10.1103/RevModPhys.73.583.

27. Ayral, T., Biermann, S., Werner, P., and Boehnke, L. (2017). Influence of Fock exchange in combined many-body perturbation and dynamical mean field

theory. Phys. Rev. B *95*, 245130. https://doi.org/10.1103/PhysRevB.95.245130.

28. In 't Veld, Y., Schüler, M., Wehling, T.O., Katsnelson, M.I., and van Loon, E.G.C.P. (2019). Bandwidth renormalization due to the intersite Coulomb interaction. J. Phys. Condens. Matter *31*, 465603. https://doi.org/10.1088/1361-648X/ab36fe.

29. Wigner, E. (1934). On the interaction of electrons in metals. Phys. Rev. *46*, 1002–1011. https://doi.org/10.1103/PhysRev.46.1002.

30. Wigner, E. (1938). Effects of the electron interaction on the energy levels of electrons in metals. Trans. Faraday Soc. *34*, 678–685. https://doi.org/10.1039/TF9383400678.

31. Lee, P.A., and Fukuyama, H. (1978). Dynamics of the charge-density wave. II. Long-range Coulomb effects in an array of chains. Phys. Rev. B *17*, 542–548. https://doi.org/10.1103/PhysRevB.17.542.

32. Ayral, T., Biermann, S., and Werner, P. (2013). Screening and nonlocal correlations in the extended Hubbard model from self-consistent combined GW and dynamical mean field theory. Phys. Rev. B *87*, 125149. https://doi.org/10.1103/PhysRevB.87.125149.

33. Yu, S.-L., and Li, J.-X. (2012). Chiral superconducting phase and chiral spin-density-wave phase in a Hubbard model on the kagome lattice. Phys. Rev. B *85*, 144402. https://doi.org/10.1103/PhysRevB.85.144402.

34. Kiesel, M.L., and Thomale, R. (2012). Sublattice interference in the kagome Hubbard model. Phys. Rev. B *86*, 121105. https://doi.org/10.1103/PhysRevB.86.121105.

35. Kiesel, M.L., Platt, C., and Thomale, R. (2013). Unconventional Fermi surface instabilities in the kagome hubbard model. Phys. Rev. Lett. *110*, 126405. https://doi.org/10.1103/PhysRevLett.110.126405.

36. Wang, W.-S., Li, Z.-Z., Xiang, Y.-Y., and Wang, Q.-H. (2013). Competing electronic orders on kagome lattices at van Hove filling. Phys. Rev. B *87*, 115135. https://doi.org/10.1103/PhysRevB.87.115135.

37. Jeong, M.Y., Yang, H.-J., Kim, H.S., Kim, Y.B., Lee, S., and Han, M.J. (2022). Crucial role of out-of-plane Sb *p* orbitals in Van Hove singularity formation and electronic correlations in the superconducting kagome metal CsV_3Sb_5. Phys. Rev. B *105*, 235145. https://doi.org/10.1103/PhysRevB.105.235145.

38. Rösner, M., Steinke, C., Lorke, M., Gies, C., Jahnke, F., and Wehling, T.O. (2016). Two-dimensional heterojunctions from nonlocal manipulations of the interactions. Nano Lett. *16*, 2322–2327. https://doi.org/10.1021/acs.nanolett.5b05009.

39. Raja, A., Chaves, A., Yu, J., Arefe, G., Hill, H.M., Rigosi, A.F., Berkelbach, T.C., Nagler, P., Schüller, C., Korn, T., et al. (2017). Coulomb engineering of the bandgap and excitons in two-dimensional materials. Nat. Commun. *8*, 15251. https://doi.org/10.1038/ncomms15251.

40. Steinhoff, A., Florian, M., Rösner, M., Schönhoff, G., Wehling, T.O., and Jahnke, F. (2017). Exciton fission in monolayer transition metal dichalcogenide semiconductors. Nat. Commun. *8*, 1166. https://doi.org/10.1038/s41467-017-01298-6.

41. Steinke, C., Wehling, T.O., and Rösner, M. (2020). Coulomb-engineered heterojunctions and dynamical screening in transition metal dichalcogenide monolayers. Phys. Rev. B *102*, 115111. https://doi.org/10.1103/PhysRevB.102.115111.

42. Sipos, B., Kusmartseva, A.F., Akrap, A., Berger, H., Forró, L., and Tutiš, E. (2008). From Mott state to superconductivity in 1T-TaS_2. Nat. Mater. *7*, 960–965. https://doi.org/10.1038/nmat2318.

43. Ang, R., Wang, Z.C., Chen, C.L., Tang, J., Liu, N., Liu, Y., Lu, W.J., Sun, Y.P., Mori, T., and Ikuhara, Y. (2015). Atomistic origin of an ordered superstructure induced superconductivity in layered chalcogenides. Nat. Commun. *6*, 6091. https://doi.org/10.1038/ncomms7091.

44. Yu, Y., Yang, F., Lu, X.F., Yan, Y.J., Cho, Y.-H., Ma, L., Niu, X., Kim, S., Son, Y.-W., Feng, D., et al. (2015). Gate-tunable phase transitions in thin flakes of 1T-TaS_2. Nat. Nanotechnol. *10*, 270–276. https://doi.org/10.1038/nnano.2014.323.

45. Wang, Y.D., Yao, W.L., Xin, Z.M., Han, T.T., Wang, Z.G., Chen, L., Cai, C., Li, Y., and Zhang, Y. (2020). Band insulator to Mott insulator transition in 1T-TaS_2. Nat. Commun. *11*, 4215. https://doi.org/10.1038/s41467-020-18040-4.

46. Wilson, J.A., Di Salvo, F.J., and Mahajan, S. (1975). Charge-density waves and superlattices in the metallic layered transition metal dichalcogenides. Adv. Phys. *24*, 117–201. https://doi.org/10.1080/00018737500101391.

47. Fazekas, P., and Tosatti, E. (1979). Electrical, structural and magnetic properties of pure and doped 1T-TaS_2. Phil. Mag. B *39*, 229–244. https://doi.org/10.1080/13642817908245359.

48. Giambattista, B., Slough, C.G., McNairy, W.W., and Coleman, R.V. (1990). Scanning tunneling microscopy of atoms and charge-density waves in 1T-TaS_2, 1T-$TaSe_2$, and 1T-VSe_2. Phys. Rev. B *41*, 10082–10103. https://doi.org/10.1103/PhysRevB.41.10082.

49. Liu, A.Y. (2009). Electron-phonon coupling in compressed 1T-TaS_2: stability and superconductivity from first principles. Phys. Rev. B *79*, 220515. https://doi.org/10.1103/PhysRevB.79.220515.

50. Ge, Y., and Liu, A.Y. (2010). First-principles investigation of the charge-density-wave instability in 1T-$TaSe_2$. Phys. Rev. B *82*, 155133. https://doi.org/10.1103/PhysRevB.82.155133.

51. Law, K.T., and Lee, P.A. (2017). 1T-TaS_2 as a quantum spin liquid. Proc. Natl. Acad. Sci. USA *114*, 6996–7000. https://doi.org/10.1073/pnas.1706769114.

52. Ribak, A., Silber, I., Baines, C., Chashka, K., Salman, Z., Dagan, Y., and Kanigel, A. (2017). Gapless excitations in the ground state of 1T-TaS_2. Phys. Rev. B *96*, 195131. https://doi.org/10.1103/PhysRevB.96.195131.

53. Klanjšek, M., Zorko, A., Žitko, R., Mravlje, J., Jagličić, Z., Biswas, P., Prelovšek, P., Mihailovic, D., and Arčon, D. (2017). A high-temperature quantum spin liquid with polaron spins. Nat. Phys. *13*, 1130–1134. https://doi.org/10.1038/nphys4212.

54. Lin, H.C., Wang, C.K., Tung, Y.C., Chiu, F.Y., Su, Y.P., Wu, J., Chen, X., and Ji, S.-H. (2020). Scanning tunneling spectroscopic study of monolayer 1T-TaS_2 and 1T-$TaSe_2$. Nano Res. *40*, 133–145. https://doi.org/10.1007/s12274-019-2584-4.

55. Darancet, P., Millis, A.J., and Marianetti, C.A. (2014). Three-dimensional metallic and two-dimensional insulating behavior in octahedral tantalum dichalcogenides. Phys. Rev. B *90*, 045134. https://doi.org/10.1103/PhysRevB.90.045134.

56. Yu, X.-L., Liu, D.-Y., Quan, Y.-M., Wu, J., Lin, H.-Q., Chang, K., and Zou, L.-J. (2017). Electronic correlation effects and orbital density wave in the layered compound 1T-TaS_2. Phys. Rev. B *96*, 125138. https://doi.org/10.1103/PhysRevB.96.125138.

57. Lee, S.-H., Goh, J.S., and Cho, D. (2019). Origin of the insulating phase and first-order metal-insulator transition in 1T-TaS_2. Phys. Rev. Lett. *122*, 106404. https://doi.org/10.1103/PhysRevLett.122.106404.

58. Petocchi, F., Nicholson, C.W., Salzmann, B., Pasquier, D., Yazyev, O.V., Monney, C., and Werner, P. (2022). Mott versus hybridization gap in the low-temperature phase of 1T-TaS2. Preprint at arXiv. https://doi.org/10.48550/arXiv.2202.01285.

59. Butler, C.J., Yoshida, M., Hanaguri, T., and Iwasa, Y. (2020). Mottness versus unit-cell doubling as the driver of the insulating state in 1T-TaS2. Nat. Commun. *11*, 2477. https://doi.org/10.1038/s41467-020-16132-9.

60. Lee, J., Jin, K.-H., and Yeom, H.W. (2021). Distinguishing a Mott insulator from a trivial insulator with atomic adsorbates. Phys. Rev. Lett. *126*, 196405. https://doi.org/10.1103/PhysRevLett.126.196405.

61. Nicholson, C.W., Petocchi, F., Salzmann, B., Witteveen, C., Rumo, M., Kremer, G., von Rohr, F.O., Werner, P., and Monney, C. (2022). Modified interlayer stacking and insulator to correlated-metal transition driven by uniaxial strain in 1T-TaS2. Preprint at arXiv. https://doi.org/10.48550/arXiv:2204.05598.

62. Fuhrmann, A., Heilmann, D., and Monien, H. (2006). From Mott insulator to band insulator: a dynamical mean-field theory study. Phys. Rev. B *73*, 245118. https://doi.org/10.1103/PhysRevB.73.245118.

63. Chen, G., Rösner, M., and Lado, J.L. (2022). Controlling magnetic frustration in 1T-TaS2 via Coulomb engineered long-range interactions. Preprint at arXiv. https://doi.org/10.48550/arXiv:2201.07826.

64. Si, Q., and Smith, J.L. (1996). Kosterlitz-thouless transition and short range spatial correlations in an extended hubbard model. Phys. Rev. Lett. *77*, 3391–3394. https://doi.org/10.1103/PhysRevLett.77.3391.

65. Smith, J.L., and Si, Q. (2000). Spatial correlations in dynamical mean-field theory. Phys. Rev. B *61*, 5184–5193. https://doi.org/10.1103/PhysRevB.61.5184.

66. Sun, P., and Kotliar, G. (2002). Extended dynamical mean-field theory and GW method. Phys. Rev. B *66*, 085120. https://doi.org/10.1103/PhysRevB.66.085120.

67. Biermann, S., Aryasetiawan, F., and Georges, A. (2003). First-principles approach to the electronic structure of strongly correlated systems: combining the GW approximation and dynamical mean-field theory. Phys. Rev. Lett. *90*, 086402. https://doi.org/10.1103/PhysRevLett.90.086402.

68. Sun, P., and Kotliar, G. (2004). Many-Body approximation scheme beyond GW. Phys. Rev. Lett. *92*, 196402. https://doi.org/10.1103/PhysRevLett.92.196402.

69. Chen, J., Petocchi, F., and Werner, P. (2022). Causal versus local GW+EDMFT scheme and application to the triangular-lattice extended Hubbard model. Phys. Rev. B *105*, 085102. https://doi.org/10.1103/PhysRevB.105.085102.

70. Mattheiss, L.F. (1973). Band structures of transition-metal-dichalcogenide layer compounds. Phys. Rev. B *8*, 3719–3740. https://doi.org/10.1103/PhysRevB.8.3719.

71. Smith, N.V., Kevan, S.D., and DiSalvo, F.J. (1985). Band structures of the layer compounds 1T-TaS_2 and 2H-$TaSe_2$ in the presence of commensurate charge-density waves. J. Phys. C Solid State Phys. *18*, 3175–3189. https://doi.org/10.1088/0022-3719/18/16/013.

72. Yan-Bin, Q., Yan-Ling, L., Guo-Hua, Z., Zhi, Z., and Xiao-Ying, Q. (2007). Anisotropic properties of TaS_2. Chin. Phys. *16*, 3809–3814. https://doi.org/10.1088/1009-1963/16/12/042.

73. Tosatti, E., and Fazekas, P. (1976). On the nature of the low-temperature phase of 1T-TaS_2. J. Phys. Colloq. *37*, C4–C168. https://doi.org/10.1051/jphyscol:1976426.

74. Brouwer, R., and Jellinek, F. (1980). The low-temperature superstructures of 1T-$TaSe_2$ and 2H-$TaSe_2$. Phys. B+C *99*, 51–55. https://doi.org/10.1016/0378-4363(80)90209-0.

75. Perfetti, L., Georges, A., Florens, S., Biermann, S., Mitrovic, S., Berger, H., Tomm, Y., Höchst, H., and Grioni, M. (2003). Spectroscopic signatures of a bandwidth-controlled Mott transition at the surface of 1T-$TaSe_2$. Phys. Rev. Lett. *90*, 166401. https://doi.org/10.1103/PhysRevLett.90.166401.

76. Perfetti, L., Loukakos, P.A., Lisowski, M., Bovensiepen, U., Berger, H., Biermann, S., Cornaglia, P.S., Georges, A., and Wolf, M. (2006). Time evolution of the electronic structure of 1T-TaS_2 through the insulator-metal transition. Phys. Rev. Lett. *97*, 067402. https://doi.org/10.1103/PhysRevLett.97.067402.

77. Marzari, N., and Vanderbilt, D. (1997). Maximally localized generalized Wannier functions for composite energy bands. Phys. Rev. B *56*, 12847–12865. https://doi.org/10.1103/PhysRevB.56.12847.

78. Souza, I., Marzari, N., and Vanderbilt, D. (2001). Maximally localized Wannier functions for entangled energy bands. Phys. Rev. B *65*, 035109. https://doi.org/10.1103/PhysRevB.65.035109.

79. Pasquier, D., and Yazyev, O.V. (2022). Ab initio theory of magnetism in two-dimensional 1T-TaS_2. Phys. Rev. B *105*, L081106. https://doi.org/10.1103/PhysRevB.105.L081106.

80. Ryee, S., Sémon, P., Han, M.J., and Choi, S. (2020). Nonlocal Coulomb interaction and spin-freezing crossover as a route to valence-skipping charge order. npj Quantum Materials *5*, 2397. https://doi.org/10.1038/s41535-020-0221-9.

81. Hüser, F., Olsen, T., and Thygesen, K.S. (2013). How dielectric screening in two-dimensional crystals affects the convergence of excited-state calculations: monolayer MoS_2. Phys. Rev. B *88*, 245309. https://doi.org/10.1103/PhysRevB.88.245309.

82. Ugeda, M.M., Bradley, A.J., Shi, S.-F., da Jornada, F.H., Zhang, Y., Qiu, D.Y., Ruan, W., Mo, S.-K., Hussain, Z., Shen, Z.-X., et al. (2014). Giant bandgap renormalization and excitonic effects in a monolayer transition metal dichalcogenide semiconductor. Nat. Mater. *13*, 1091–1095. https://doi.org/10.1038/nmat4061.

83. Kim, T.J., Ryee, S., Han, M.J., and Choi, S. (2020). Dynamical mean-field study of Vanadium diselenide monolayer ferromagnetism. 2D Mater. *7*, 035023. https://doi.org/10.1088/2053-1583/ab8b48.

84. Boix-Constant, C., Mañas-Valero, S., Córdoba, R., Baldoví, J.J., Rubio, Á., and Coronado, E. (2021). Out-of-Plane transport of 1T-TaS_2/graphene-based van der Waals heterostructures. ACS Nano *15*, 11898–11907. https://doi.org/10.1021/acsnano.1c03012.

85. Karbalaee Aghaee, A., Belbasi, S., and Hadipour, H. (2022). Ab initio calculation of the effective Coulomb interactions in MX_2 (M=Ti, V, Cr, Mn, Fe, Co, Ni; X= S, Se, Te): intrinsic magnetic ordering and Mott phase. Phys. Rev. B *105*, 115115. https://doi.org/10.1103/PhysRevB.105.115115.

86. Kamil, E., Berges, J., Schönhoff, G., Rösner, M., Schüler, M., Sangiovanni, G., and Wehling, T.O. (2018). Electronic structure of single layer 1T-$NbSe_2$: interplay of lattice distortions, non-local exchange, and Mott–Hubbard correlations. J. Phys. Condens. Matter *30*, 325601. https://doi.org/10.1088/1361-648X/aad215.

87. Miyake, T., Nakamura, K., Arita, R., and Imada, M. (2010). Comparison of ab initio low-energy models for LaFePO, LaFeAsO, $BaFe_2As_2$, LiFeAs, FeSe, and FeTe: electron correlation and covalency. J. Phys. Soc. Jpn. *79*, 044705. https://doi.org/10.1143/JPSJ.79.044705.

88. Nakata, Y., Sugawara, K., Chainani, A., Oka, H., Bao, C., Zhou, S., Chuang, P.-Y., Cheng, C.-M., Kawakami, T., Saruta, Y., et al. (2021). Robust charge-density wave strengthened by electron correlations in monolayer 1T-$TaSe_2$ and 1T-$NbSe_2$. Nat. Commun. *12*, 5873. https://doi.org/10.1038/s41467-021-26105-1.

89. Jarrell, M., and Gubernatis, J.E. (1996). Bayesian inference and the analytic continuation of imaginary-time quantum Monte Carlo data. Phys. Rep. *269*, 133–195. https://doi.org/10.1016/0370-1573(95)00074-7.

90. Sim, J.-H., and Han, M.J. (2018). Maximum quantum entropy method. Phys. Rev. B *98*, 205102. https://doi.org/10.1103/PhysRevB.98.205102.

91. Yoon, H., Sim, J.-H., and Han, M.J. (2018). Analytic continuation via domain knowledge free machine learning. Phys. Rev. B *98*, 245101. https://doi.org/10.1103/PhysRevB.98.245101.

92. Ritschel, T., Berger, H., and Geck, J. (2018). Stacking-driven gap formation in layered 1T-TaS_2. Phys. Rev. B *98*, 195134. https://doi.org/10.1103/PhysRevB.98.195134.

93. Mañas-Valero, S., Huddart, B.M., Lancaster, T., Coronado, E., and Pratt, F.L. (2021). Quantum phases and spin liquid properties of 1T-TaS2. npj Quantum Mater *6*, 1–9. https://doi.org/10.1038/s41535-021-00367-w.

94. Kresse, G., and Hafner, J. (1993). Ab initio molecular dynamics for open-shell transition metals. Phys. Rev. B *48*, 13115–13118. https://doi.org/10.1103/PhysRevB.48.13115.

95. Kresse, G., and Furthmüller, J. (1996). Efficiency of ab-initio total energy calculations for metals and semiconductors using a plane-wave basis set. Comput. Mater. Sci. *6*, 15–50. https://doi.org/10.1016/0927-0256(96)00008-0.

96. Choi, S., Semon, P., Kang, B., Kutepov, A., and Kotliar, G. (2019). ComDMFT: a massively parallel computer package for the electronic structure of correlated-electron systems. Comput. Phys. Commun. *244*, 277–294. https://doi.org/10.1016/j.cpc.2019.07.003.

97. Nakamura, K., Yoshimoto, Y., Nomura, Y., Tadano, T., Kawamura, M., Kosugi, T., Yoshimi, K., Misawa, T., and Motoyama, Y. (2021). RESPACK: an ab initio tool for derivation of effective low-energy model of material. Comput. Phys. Commun. *261*, 107781. https://doi.org/10.1016/j.cpc.2020.107781.

98. Perdew, J.P., Burke, K., and Ernzerhof, M. (1996). Generalized gradient approximation made simple. Phys. Rev. Lett. *77*, 3865–3868. https://doi.org/10.1103/PhysRevLett.77.3865.

STAR★METHODS

KEY RESOURCES TABLE

REAGENT or RESOURCE	SOURCE	IDENTIFIER
Software and algorithms		
VASP	Georg Kresse et al.[94,95]	https://www.vasp.at/
ComDMFT	Sangkook Choi et al.[96]	https://github.com/comscope/ComDMFT
RESPACK	Kazuma Nakamura et al.[97]	https://sites.google.com/view/kazuma7k6r

RESOURCE AVAILABILITY

Lead contact

Further information and requests for resources should be directed to and will be fulfilled by the lead contact, Myung Joon Han (mj.han@kaist.ac.kr).

Materials availability

This study did not generate new unique reagents.

Data and code availability

All data reported in this paper will be shared by the lead contact (mj.han@kaist.ac.kr) upon reasonable request.

This study did not report original code.

Any additional information required to reanalyze the data reported in this work paper is available from the lead contact upon reasonable request.

METHOD DETAILS

DFT and extended hubbard model construction

We performed DFT calculations of monolayer 1T- and CCDW-TaS_2 with Vienna Ab initio Simulation Package (VASP).[94,95] The cell parameters and the internal coordinates were optimized with the force criterion of 0.1 meV/Å. The GGA-PBE functional[98] was used and the 25Å vacuum taken into account to simulate the monolayer. 21×21×1 (8× 8× 1) k-grid and 500 eV (400 eV) cutoff energy were adopted for 1T-TaS_2 (CCDW-TaS_2). To describe the effect of electronic correlations of low-energy state in CCDW-TaS_2, we consider the single-band extended Hubbard model:

$$H = -\sum_{ij\sigma} t_{ij} c^{\dagger}_{i\sigma} c_{j\sigma} + U\sum_{i} n_{i\uparrow} n_{i\downarrow} + V\sum_{<ij>} n_i n_j - \mu\sum_{i} n_i \qquad \text{(Equation 7)}$$

where $c^{\dagger}_{i\sigma}$ and $c_{i\sigma}$ is the creation and annihilation operator of electron, respectively, with spin $\sigma = \{\uparrow, \downarrow\}$ at site i. $n_i = c^{\dagger}_{i\sigma} c_{i\sigma}$ is the electron number operator at site i, and $\sum_{<ij>}$ denotes the nearest-neighbor summation. The hopping amplitude t_{ij} between two site i and j was calculated with the MLWF method.[77,78] U and V is the local and non-local Coulomb interaction, respectively. The realistic estimation of these two interaction parameters is one of the main issues of current study. For this purpose, we used (c)RPA method as implemented in RESPACK code.[97]

GW + EDMFT

The Hamiltonian is solved within GW + EDMFT whose standard self-consistent loop can be briefly summarized as below.[27,32]

(i) Calculate the lattice green function G and the screened Coulomb interaction W:

$$G(k, i\omega_n) = [i\omega_n - t(k) + \mu - \Sigma(k, i\omega_n)]^{-1},$$

$$W(q, i\Omega_m) = v(q)[1 - v(q)P(q, i\Omega_m)]^{-1},$$

where k and q are the crystal momentum vectors. $i\omega_n$ and $i\Omega_m$ refers to the fermionic and bosonic Matsubara frequency, respectively. The momentum space t(k) corresponds to the Fourier transformed t_{ij}. $\Sigma(k, i\omega_n)$ and $P(q, i\Omega_m)$ represents the electron self-energy and the polarization function, respectively. The bare Coulomb interaction v(q) is given by $v(q) = 2V\left[\cos(q_x) + \cos\left(\frac{1}{2}q_x + \frac{\sqrt{3}}{2}q_y\right) + \cos\left(-\frac{1}{2}q_x + \frac{\sqrt{3}}{2}q_y\right)\right]$. In practice, we start the first loop from $\Sigma(k, i\omega_n) = P(q, i\Omega_m) = 0$.

(ii) Compute the fermionic and bosonic Wiess fields $\mathcal{G}$ and $\mathcal{U}$:

$$\mathcal{G}(i\omega_n) = \left[G_{loc}(i\omega_n)^{-1} + \Sigma_{loc}(i\omega_n)\right]^{-1},$$

$$\mathcal{U}(i\Omega_m) = \left[W_{loc}(i\omega_n)^{-1} + P_{loc}(i\Omega_m)\right]^{-1},$$

where $A_{loc}(i\omega_n) = \frac{1}{N_k}\sum_k A(k, i\omega_n)$ for any *A*, and N_k is the number of *k*-points.

(iii) Solve the following impurity model to obtain the impurity self-energy $\Sigma_{imp}(i\omega_n)$ and polarization $P_{imp}(i\Omega_m)$:

$$S_{imp} = \int_0^\beta \int d\tau d\tau' \bar{c}(\tau)\left[-\mathcal{G}^{-1}(\tau - \tau')\right]c(\tau')$$

$$+\frac{1}{2}\int_0^\beta \int d\tau d\tau' \mathcal{U}(\tau - \tau')n(\tau)n(\tau')$$

where $A(\tau)$ is the Fourier transormation of $A(i\omega_n)$, and $\bar{c}(\tau)$ and $c(\tau)$ are the Grassmann field for electrons. Here we took the continuous-time hybridization expansion quantum Monte Carlo impurity solver as implemented in ComDMFT package.[96]

(iv) Construct the new self-energy and polarization function from the calculated $\Sigma_{imp}(i\omega_n)$ and $P_{imp}(i\Omega_m)$:

$$\Sigma(k, i\omega_n) = \Sigma_{imp}(i\omega_n) + \Sigma^{GW}_{nonloc}(k, i\omega_n),$$

$$P(q, i\Omega_m) = P_{imp}(i\Omega_m) + P^{GW}_{nonloc}(q, i\Omega_m),$$

where $\Sigma^{GW}(k, i\omega_n) = -\sum_{q, i\Omega_m} G(k + q, i\omega_n + i\Omega_m)W(q, i\Omega_m)$,

$$P^{GW}(q, i\Omega_m) = 2\sum_{k, i\omega_n} G(k + q, i\omega_n + i\Omega_m)G(k, i\omega_n),$$

and

$$A_{nonloc}(k, i\omega_n) = A(k, i\omega_n) - A_{loc}(i\omega_n).$$

(v) Go back to the step (i) and repeat the calculations until $G(k, i\omega_n)$ and $W(q, i\Omega_m)$ are converged.